Journal Name

ARTICLE

Broad temperature plateau for high ZTs in heavily doped p-type SnSe single crystals†

Received 00th January 20xx,
Accepted 00th January 20xx

DOI: 10.1039/x0xx00000x

www.rsc.org/

Kunling Peng,[a,b] Xu Lu,[a] HengZhan,[a] Si Hui,[c] Xiaodan Tang,[a,b] Guiwen Wang,[a,b] Jiyan Dai,[d] Ctirad Uher,[c] Guoyu Wang,*[b] Xiaoyuan Zhou.*[a]

Excellent thermoelectric performance is obtained over a broad temperature range from 300 K to 800 K by doping single crystals of SnSe. The average value of the figure of merit *ZT* of more than 1.17 is measured from 300 K to 800 K along the crystallographic b-axis of 3 at% Na-doped SnSe, with the maximum *ZT* reaching a value of 2 at 800 K. Room temperature value of the power factor for the same sample and in the same direction is 2.8 mW/mK^2, which is an order of magnitude higher value than for the undoped crystal. Calculations show that Na doping lowers the Fermi level and increases the number of carrier pockets in SnSe, leading to a collaborative optimization of the Seebeck coefficient and the electrical conductivity. The resultant optimized carrier concentration and the increased number of carrier pockets near the Fermi level in Na-doped samples are believed to be the key factors behind the spectacular enhancement of the average *ZT*.

1. Introduction

To satisfy energy demands in a modern society, the focus has shifted towards utilizing green technologies and alternative energy sources so as to reduce the dependence on fossil fuels. Thermoelectric (TE) devices which can serve as heat pumps or recover waste heat to generate electrical power, are one of the promising candidates[1,2]. The efficiency of thermoelectric materials is determined by the dimensionless figure of merit *ZT*, defined as $ZT=S^2\sigma T/\kappa$, where *S* is the Seebeck coefficient, σ is the electrical conductivity, $S^2\sigma$ is the power factor (*PF*) and κ is the thermal conductivity consisting of the lattice conductivity (κ_l) and the electronic conductivity (κ_e). To achieve high *ZT*, several general strategies have emerged in the past two decades. One of them is band engineering which is implemented by the convergence of electronic bands[3,4], distortions in the electronic density of states (DOS)[5], and alignments of the valence or conduction bands[6]. Another strategy is structural engineering which includes designing new compounds with complex crystal structures[7,8], introducing nanostructures and developing lower-dimensional materials[9]. Such approaches are typically used with the polycrystalline thermoelectric materials. In contrast, single crystals are rarely used as thermoelectric materials primarily because they are fragile, often easily cleave and, due to the absence of grain boundaries, single crystals possess high thermal conductivity.

Currently, there is much interest in exploring thermoelectric properties of two bulk single-crystalline structures: SnSe[10,11] and In_4Se_3[12], both of which are actually quasi-laminar structures.

SnSe is a compound consisting of Earth-abundant and environmentally friendly elements and has recently been shown to have an ultrahigh thermoelectric performance with the maximum *ZT* of 2.6 reached at 923 K along the b-axis[10]. However, this exceptionally high peak value of *ZT* is found in the high-temperature phase of SnSe (T>800K, Cmcm space group #63, a=4.31Å, b=11.70Å, c=4.31Å)[13], while the thermoelectric performance of the low-temperature phase (T<800K, Pnma space group #62, a=11.49Å, b=4.44Å, c=4.135Å) is rather poor, which greatly limits applications of this material.

In this paper we demonstrate an excellent thermoelectric performance achieved in doped Sn(Na, Ag)Se single crystals over a broad range of temperatures with the average *ZT* value well in excess of unity from room temperature to 800 K where the maximum *ZT* attains values of 2 or better. Our work focuses on the performance along the *b* direction in SnSe, where the best results have been reported previously. For comparison, the average *ZT* we obtain in a single crystal of $Sn_{97}Na_3Se_{100}$ along the *b*- axis is greatly enhanced and is about 1.5 times larger than that of the undoped SnSe crystal in the same direction. Based on our theoretical estimates and the experimental data, we find that the Fermi level can be shifted to the desired range of energies by doping with Na or Ag and this greatly improves the overall thermoelectric performance and makes SnSe single crystals useful over a very wide range of temperatures.

2. Experimental and theoretical methods

---

[a] *College of Physics, Chongqing University, Chongqing 401331, People's Republic of China. Corresponding author: xiaoyuan2013@cqu.edu.cn*

[b] *Chongqing Institute of Green and Intelligent Technology, Chinese Academy of Sciences, Chongqing 400714, People's Republic of China. Corresponding author: guoyuw@cigit.ac.cn*

[c] *Department of Physics, University of Michigan, Ann Arbor MI 48109, USA.*

[d] *Department of Applied Physics, The Hong Kong Polytechnic University Kowloon, Hong Kong.*

†Electronic Supplementary Information (ESI) available. See DOI: 10.1039/x0xx00000x

2.1. Synthesis

Elemental constituents were weighed according to the stoichiometry of $Sn_{1-x}R_xSe$ (R=Na,Ag; x=0, 1, 2, 3) and loaded into quartz tubes under argon atmosphere and sealed at 5×10^{-4} Pa. The quartz tubes were heated up to 1273K over 12h, kept at that temperature for 10h, and subsequently furnace cooled to room temperature. The obtained ingots (~15*g*) were crushed into a powder and sealed again in a cone-shaped quartz tube under argon. Single crystals were grown by a modified Bridgeman method. The presence of argon gas during the growth protects the crystal from oxidation because the cone-shaped quartz tubes often break as the structure undergoes a phase transition from the *Cmcm* to the *Pnma* phase. Excellent single crystalline ingots of $Sn_{1-x}R_xSe$ with the diameter of 13mm and the height of 15mm were obtained.

2.2. Measurements

The obtained single crystal ingots were cut into ~9mm×3mm×2mm rectangular-shaped samples for electrical property measurements and square planar samples of ~6mm×6mm×1.5mm for thermal conductivity measurements. Electrical conductivity and the Seebeck coefficient were measured using a *LSR-3* (*Linseis, Germany*) instrument under a static helium atmosphere. Thermal diffusivity (*D*) was obtained on a *LFA 457* (*Netzsch, Germany*) and the specific heat capacity was used as suggested by reference 6, which is comparable to the reported values[14]. The thermal conductivity was calculated from $\kappa=\rho DC_p$, where ρ is the density. The combined uncertainly for all measurements involved in the calculation of *ZT* is around 15%. The lattice thermal conductivity was obtained by subtracting the electronic thermal conductivity κ_e from the total thermal conductivity, $\kappa_l=\kappa-\kappa_e$, using the Wiedemann–Franz law, $\kappa_e=\sigma LT$, where *L* is the Lorenz constant. Due to the complexity and the non-parabolicity of the valence band structure around the Fermi level for p-type SnSe, accurate determination of the *L* is difficult. An estimation of L was made using a single parabolic band (SPB) model with acoustic phonon scattering, resulting in an L with a deviation of less than 10% as compared with a more rigorous single non-parabolic band and multiple band models calculation[15,16]. Irrespective of the value employed for the Lorenz constant, this will not affect the total thermal conductivity, the final *ZT*, and the conclusion in this work.

The temperature-dependent Hall coefficient was measured using 16 Hz low-frequency excitations with a Linear Research *AC* Resistance Bridge *(LR-700*) in the applied field of ±1 T generated by an air-bore *Oxford* superconducting magnet accommodating a tubular oven with a Hall-probe insert. Crystal structures were determined using an X-ray single crystal diffractometer (*SuperNova, Agilent*) and transmission electron microscopy studies were carried out using *a JEOL 2100F* microscope.

2.3. Density function theory (DFT) calculations.

Projector augmented plane wave (PAW) method[17,18] as implemented in the Vienna *ab initio* simulation package (VASP)[19] code was used for structural relaxation. The exchange-correlation functional was defined using a generalized gradient approximation (GGA) of Perdew–Burke–Ernzerhof (PBE)[20]. Supper cells (2×2×2, *Pnma* and *Cmcm*) with 64 atoms were built for the purpose of randomly replacing Sn atoms with Na or Ag atoms corresponding to the doping amount of ~3 percent. The cut-off energy in the plane wave expansion was set at 500eV. The atomic positions were relaxed until the forces on the atoms were smaller than 0.01eV/Å. For the Brillouin zone integrations, we used the Monkhorst–Pack k-mesh scheme with 3×5×5 for *Pnma* when calculating the total energy and 7×13×13 for *Pnma* when calculating the DOS. Another supper cell (1×5×5, *Pnma*) with 200 atoms was built to calculate the Fermi level for $Sn_{1-x}Na_xSe$ (x=0, 0.01, 0.02, 0.03, 0.04) without relaxing the supper cell but the primitive cell in the *Pnma* structure.

3. Results and discussion

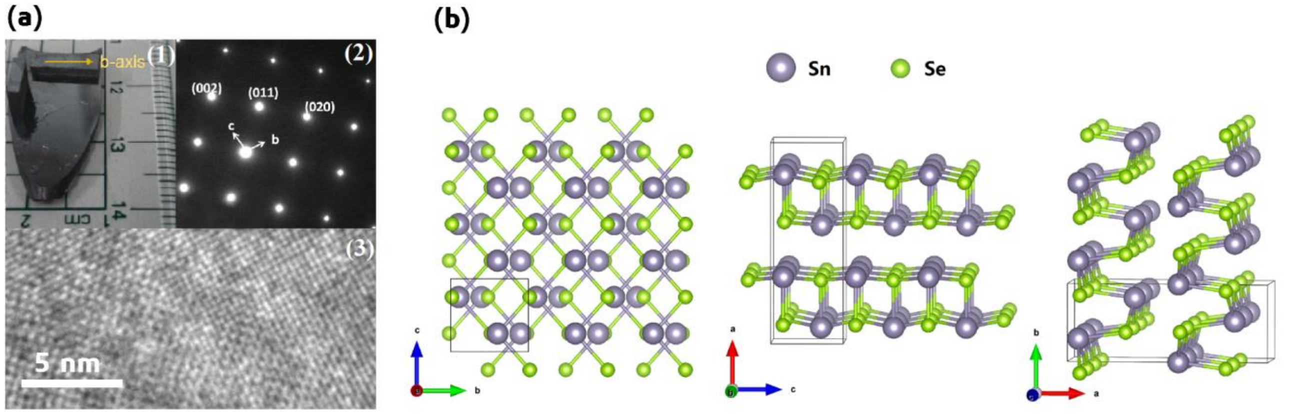

Figure 1. The crystal structure of SnSe. (a) High-resolution TEM images of a single crystal of $Sn_{0.97}Na_{0.03}Se$ and the electron diffraction pattern along the [100] direction (inset) at room temperature; (b) the *Pnma* structure based on the single crystal diffraction data of $Sn_{0.97}Na_{0.03}Se$.

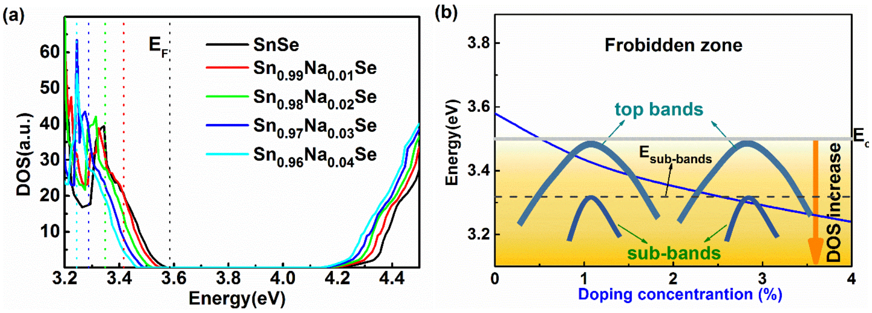

Figure 2. Density of states in the *Pnma* phase of SnSe. (a) The total DOS of $Sn_{1-x}Na_xSe$ (x=0, 0.01, 0.02, 0.03, 0.04) in the *Pnma* structure. The valance band edge is at 3.5±0.05eV for all samples in calculations; (b) the Fermi level as a function of doping concentration and temperature in the *Pnma* structure. The blue line shows the Fermi level as a function of Na doping concentration which can also apply qualitatively to other dopants in SnSe. (The top bands refer to VB1 or VB2; the sub-bands refer to VB3 or VB4, see also Figure 3).

3.1. Crystal structure characterization

To confirm that the obtained samples are single crystals, XRD analysis and transmission electron microscopy (TEM) were carried out. Figure 1 shows nice single crystal cleavage faces along the b-c plane (Figure 1a, inset 1), an electron diffraction pattern (Figure 1a, inset 2), a high-resolution TEM image (Figure 1a, inset 3), and the interpretation of the XRD single crystal diffraction data (Figure 1b). The high-resolution TEM image of the single crystal $Sn_{0.97}Na_{0.03}Se$ shows a well-organized crystal lattice and unit cells projected along the [100] direction can be identified, while the electron diffraction pattern along the [100] direction can be readily indexed to the SnSe structure at room temperature. The crystal structure of SnSe based on the single crystal diffraction data is shown in Figure 1b and confirms that the structure belongs to the *Pnma* space group (a=11.493Å, b =4.152Å, c= 4.438Å).

3.2. Electronic structure calculations

Calculated Fermi levels for the crystals doped with 1%, 2%, 3%, and 4% of Na are shown in Figure 2a. It is apparent that the Fermi level is lowered when the content of Na increases, and the top of the valance band remains at around 3.5eV; the result is depicted by the blue solid line in Figure 2b, where the top bands refer to VB1 or VB2 and the sub-bands refer to VB3 or VB4, see also Figure 3.

The first row of panels in Figure 3 indicates that the DOS near the Fermi level is derived from the s- and p-orbitals of Sn and especially from the p-orbitals of Se. The contribution of the doping elements Na and Ag to the DOS is almost negligible. However, the doping elements change the profile of the original DOS by increasing the number of carrier pockets near the Fermi level (see also Figure 2b). As is well known, the increase in the local DOS near the Fermi level can greatly enhance the Seebeck

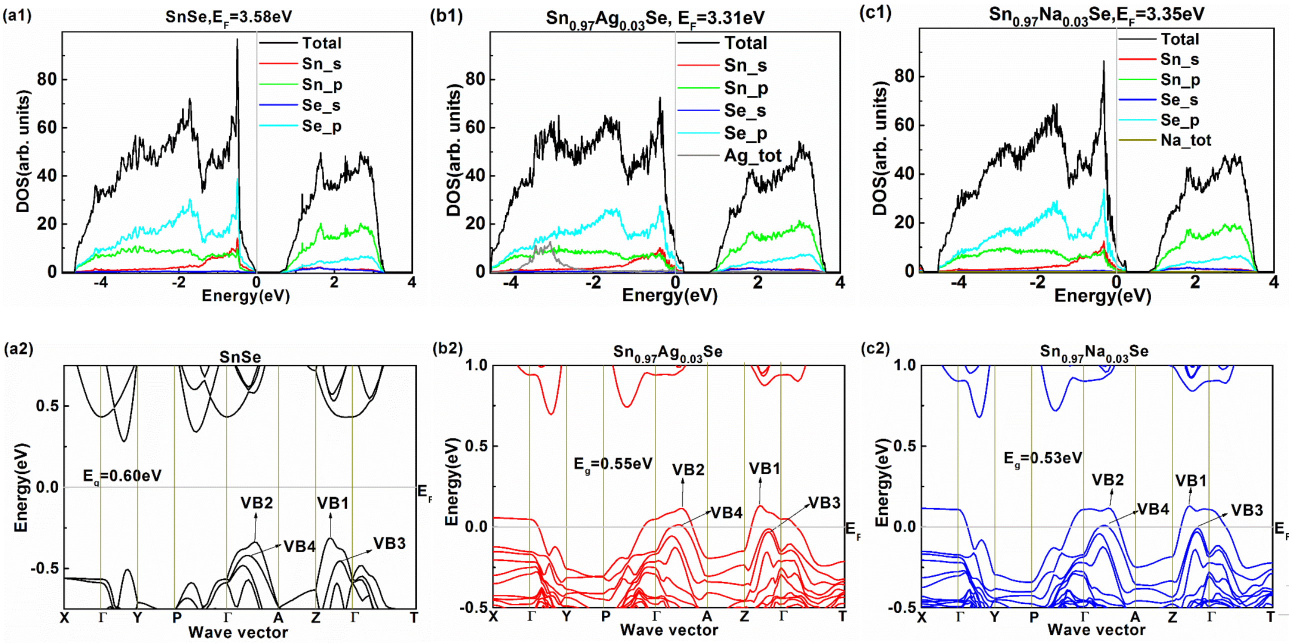

Figure 3. Electronic band structure and DOS for the *Pnma* structure with super cell.

coefficient which for a degenerate system, is given by the Mott expression[21]

$$S=\frac{\pi^2}{3}\frac{k_B^2T}{q}\left\{\frac{dn(E)}{n\,dE}+\frac{d\mu(E)}{\mu\,dE}\right\}_{E=E_F} \quad (1)$$

with

$$n[E]=g[E]f[E] \quad (2)$$

where k_B is the Boltzmann constant, *f(E)* is the Fermi function, q is the carrier charge, *n(E)* is the carrier concentration, *μ(E)* is the carrier mobility, and *g(E)* is the density of states (DOS). Thus, the Seebeck coefficient *S* depends on the energy derivative of the density of states, which increases via doping compared to that of the undoped sample[5]. Based on the total DOS analysis, we can also qualitatively understand that the carrier concentration (*p(E)*) depends on the energy derivative of the energy-dependent DOS, which largely increases via doping compared to that of the undoped sample, yielding an increase in the carrier concentration as well as in the electrical conductivity as the Na and Ag doping content increases, as shown in Figure 4b and 4a, respectively.

Doping modifies the band structure of the Pnma phase of SnSe in two major ways: it shifts the position of the Fermi level and it tends to flatten the top of the valence band, both effects illustrated in Figure 3. The shift of the Fermi level upon doping is significant and, for high enough doping content (such as 3% of Ag or Na), the Fermi level enters the valence band, turning the structure into a metal. At the same time, the flattened valence band edge upon doping, especially when Na is used, gives rise to, via Eq.3, an enhanced effective mass and thus Na and Ag doping increases the band effective mass of holes.

$$\frac{1}{\hbar^2}\left(\frac{\partial^2E}{\partial k^2}\right)_{k=k_i}=\frac{1}{m^*} \quad (3)$$

In Eq.3, is the Planck constant and k_i is the wavevector of the *i*-th carrier pocket. Moreover, the band gap slightly narrows upon doping. It is worth noting that, in sufficiently doped samples, in addition to the carrier pockets at the top of the valence band (e.g. VB1, VB2 in Figure 3), the carrier pockets of the lower lying valence bands (e.g. VB3, VB4 in Figure 3) may also contribute to the electronic transport[22, 23].

As discussed in ref.1, 22, the increase in carrier pockets near the Fermi level (when multiple bands have the same or comparable energy within a few k_BT) can enhance the Seebeck coefficient. Here we list some differences in the band energy (see Figure 3): △E(VB1-VB2) = 0.020 eV, △E(VB4-VB3) = 0.038 eV for pure sample; △E(VB2-VB1) = 0.017 eV, △E(VB4-VB3) = 0.028 eV for $Sn_{0.97}Ag_{0.03}Se$; △E(VB2-VB1) = 0.011 eV, △E(VB4-VB3) = 0.022 eV for $Sn_{0.97}Na_{0.03}Se$. Furthermore, theoretical calculations show that the number of carrier pockets in sub-bands is 6, indicating that a high multiple carrier pockets is achieved near the Fermi level through doping and the Seebeck coefficient should be enhanced.

3.3. Electronic transport properties

Temperature dependence of the electrical conductivity (σ), the carrier concentration, the Seebeck coefficient, and the power factor are presented in Figure 4. The electrical conductivity in Figure 4a shows two distinct regions of conduction. At low temperatures the electrical conductivity shows a metallic character with the conductivity decreasing as the temperature increases. At high temperatures, thermal activation of charge carriers takes place and the electrical conductivity increases with increasing temperature. The cross over between the two regimes of conduction depends on the degree of doping. One can also see that the electrical conductivity of the Na and Ag doped single crystals is at least an order of magnitude higher than the conductivity of the pure SnSe crystal. It should be noted that all Na-doped samples show at least 50 times higher electrical conductivity at room temperature than the undoped crystal. As shown in Figure 2b, the Inverse R_H of $Sn_{0.99}Na_{0.01}Se$ and $Sn_{0.98}Na_{0.02}Se$ (Figure 4b) are indeed high, which naturally indicates the high electrical conductivity in Na-doped samples. More importantly, besides the contribution from the increased carrier concentration, the high electrical conductivity benefits from the higher total DOS near Fermi level as discussed in relation to Figure 2 and 3. One also notes in Figure 4 that the electrical conductivity of the Na-doped crystal is much higher than that of the Ag-doped crystal at the same doping level. This we attribute to different valence states of the two dopants and their effect on electron scattering.

Because all doped single crystals in the low temperature region show a linear relationship between the logarithm of conductivity (base of 10) and the temperature rather than the conductivity falling approximately inversely with the temperature if truly metallic, this implies that the carrier concentration decreases as the temperature increases. This is, indeed, confirmed by Hall effect measurements shown in Figure 4b where the carrier density of $Sn_{0.99}Na_{0.01}Se$ and $Sn_{0.98}Na_{0.02}Se$ crystals decreases rapidly with the rising temperature, the trend distinctly different from that observed in other popular TE materials (see Figure 4b, insert[5, 24]). The decrease in the carrier concentration means that the DOS decreases. Eventually, at elevated temperatures, an activated (semiconducting) behavior sets in. We believe that the Fermi level shifts with the temperature and the red line in Figure 4c indicates schematically this trend.

Figure 4d shows the Seebeck coefficient of all samples. Doped single crystals have a rather small Seebeck coefficient and Na-doped crystals have a smaller Seebeck coefficient than Ag-doped crystals of comparable doping content. We also note that the Seebeck coefficient of $Sn_{0.99}Na_{0.01}Se$ is larger than that of $Sn_{0.98}Na_{0.02}Se$ and $Sn_{0.97}Na_{0.03}Se$, the latter two crystals having comparable values. Nevertheless, all doped SnSe crystals, regardless of whether Ag or Na doped, lie well above the Pisarenko line[25] in Figure 4e. We attribute this to the beneficial effect of multiple carrier pockets in the doped SnSe crystals. In addition, the deviation from the Pisarenko line indicates that the single band model is not adequate for this material and multi-band model is necessary for accurate theoretical fitting. Although the Seebeck coefficient of Na-doped crystals is distinctly smaller than the Seebeck coefficient of Ag-doped crystals, see Figures 4d and 4e, the much higher

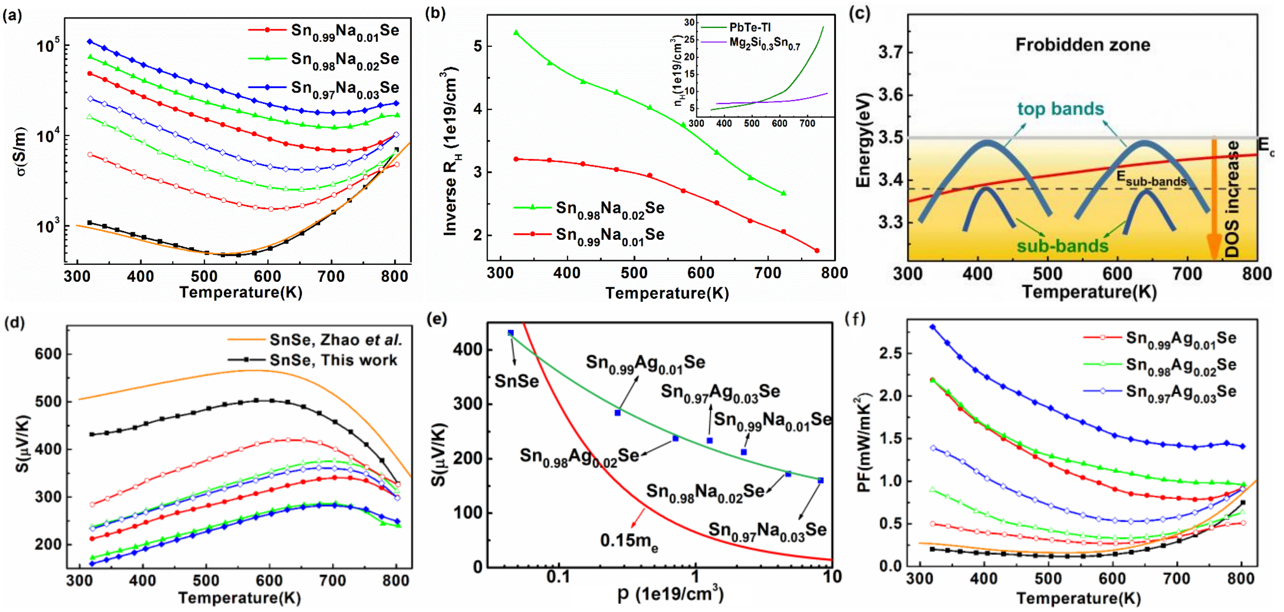

Figure 4. Temperature dependence of electronic transport properties. (a) electrical conductivity; (b) inverse R_H of $Sn_{0.99}Na_{0.01}Se$ and $Sn_{0.98}Na_{0.02}Se$ that give an indication of the carrier concentration; (c) the Fermi level as a function of temperature in the *Pnma* structure illustrated by the red line. The heavy bands refer to VB1 or VB2; the light bands refer to VB3 or VB4 (see Figure 3); (d) Seebeck coefficient; (e) the Pisarenko relation given by the red solid line (Seebeck coefficient vs. carrier concentration) assuming a single parabolic band model at room temperature compared to the estimated results measured on all $Sn_{1-x}R_xSe$ samples (blue dot or green fitting line) of this study. The difference between the red line and the green line indicates that the single band model is not adequate for this material; (f) the power factor.

electrical conductivity of the former yields much larger power factors compared to the Ag-doped SnSe crystals. This is illustrated by Figure 4f, where the power factor of all crystals is plotted against the temperature. The highest Na-doped crystal, $Sn_{0.97}Na_{0.03}Se$, shows excellent electronic properties with the power factor of more than 1.38 mW/mK^2 in the whole temperature range and the power factor as high as 2.8 mW/mK^2 at room temperature. Compared to other thermoelectric materials, the power factor achieved in the $Sn_{0.97}Na_{0.03}Se$ crystal is quite high and competes very favorably with efficient thermoelectric materials such as PbTe[26], $Mg_2Si_{1-x}Sn_x$[24,27], $Fe_xCo_{1-x}Sb_3$[28], and Bi_3Te_4[29]. Based on the previous discussion, we attribute the large enhancement in the power factor of $Sn_{0.97}Na_{0.03}Se$ to the presence of multiple carrier pockets and the lowered Fermi level.

3.4. Thermal transport properties

The temperature dependence of the total thermal conductivity (κ) for all samples is shown in Figure 6a. The total thermal conductivity of all samples is in the range between 1.78 and 2.24W/mK at room temperature, confirming the result of previous studies (around 1.8 W/mK)[11]. The lattice thermal conductivity (κ_l) is calculated by subtracting the electronic part from the total thermal conductivity as shown in Figure 6b. The values of κ_l are quite low and similar to polycrystalline samples of other important families of thermoelectric materials such as PbTe[26], $Mg_2Si_{1-x}Sn_x$[24,27], $Fe_xCo_{1-x}Sb_3$[28]. The lattice thermal conductivity follows approximately the 1/T temperature dependence characteristic of the dominance of Umklapp phonon processes[30]. Apparently, a strong bonding anharmonicity[10] contributes to such low lattice thermal conductivities. Ag-doping shows little effect on the lattice

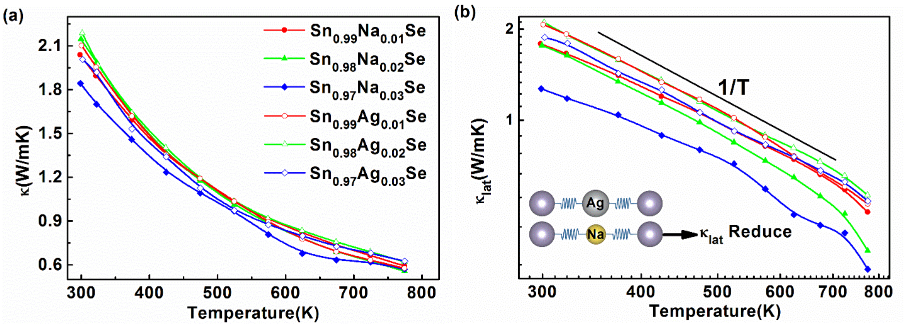

Figure 6. The thermal properties as a function of temperature. (a), thermal conductivity. (b), lattice thermal conductivity.

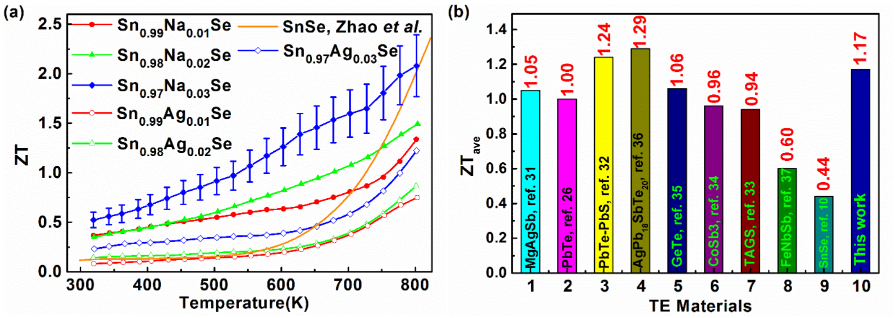

Figure 7. Figure of merit. (a) Figure of merit in this paper; (b) *ZT* values for several popular TE materials with the red numbers indicating the average *ZT* value ranging from 300 to 800 K for each material (MgAgSb only from 300 to 550 K). Clearly, doped SnSe single crystals are very promising.

thermal conductivity. This is understandable in view of a similar size and mass of Ag and Sn atoms and therefore a minimal effect on the scattering of phonons. A very different situation arises in the case of Na-doped SnSe where Na and Sn have very different sizes and masses (see an inset in Figure 6b) and thus the mass- and size-dependent scattering of phonons is significant. This is clearly seen in Figure 6b, where with the increasing content of Na the lattice thermal conductivity decreases quite markedly.

3.5. Overall figure of merit

The figure of merit was calculated based on the experimental data of the relevant transport parameters. As compared to the undoped sample reported by Zhao et al., which previously provided the record-high *ZT* values[10], Na-doped SnSe crystals possess a higher figure of merit, especially the heaviest doped $Sn_{0.97}Na_{0.03}Se$. Only at temperatures above 800 K, does this undoped SnSe exceed the figure of merit of the $Sn_{0.97}Na_{0.03}Se$ crystal. The performance of Na-doped single crystals is also much better than that of Ag-doped SnSe. The difference in the performance derives mainly from the superior electronic properties of Na-doped crystals. Over the temperature range from 300 K to 800 K, the average *ZT* value of 1.17 is obtained for the $Sn_{0.97}Na_{0.03}Se$ crystal, indeed, an excellent and highly competitive value compared to the best results of currently explored TE materials[10, 26, 31-38]. All the above results show that $Sn_{0.97}Na_{0.03}Se$ is a very promising TE material over a broad range of temperatures with a good thermal stability (see Figure S5). As the previous studies have shown, SnSe can be used to temperatures approaching 950 K and thus even higher average values over a broader range of temperatures are likely.

4. Conclusions and outlook

Combining theoretical calculations with experimental studies, we explored the effect of doping SnSe single crystals with two distinct elements, Na and Ag. Calculations show that the Fermi level is shifted upon doping, the valence band edge is flattened, and the number of carrier pockets is enlarged, all three effects having a positive influence on the electronic transport and thermoelectric properties of doped SnSe along the b-axis, the direction where the performance is maximized. Moreover, a significantly different mass and size of Na atoms compared to atoms of Sn, gives rise to a strong mass and size defect scattering of phonons which reduces the lattice thermal conductivity quite markedly. The overall effect is an excellent power factor and the figure of merit which extend over a broad range of temperatures. This is particularly the case of $Sn_{0.97}Na_{0.03}Se$ where the average ZT value over the temperature range of 300 K to 800 K reaches well over unity and the figure of merit at 800 K is in excess of 2. Coupled with their non-toxic nature and no major environmental concerns, doped SnSe crystals offer excellent thermoelectric performance over a very broad range of temperatures.

Acknowledgement

The work is financially supported in part by the National Natural Science Foundation of China (Grant no. 11344010, 11404044, 51472036), the Fundamental Research Funds for the Central Universities (CQDXWL-2013-Z010). This work also at the Chongqing Institute of Green and Intelligent Technology, Chinese Academy of Sciences is supported by the One Hundred Person Project of the Chinese Academy of Science, Grant No. 2013-46. CU and HS acknowledge support from CERC-CVC, the joint US-China Program supported by the U.S. Department of Energy, under the Award Number DE-PI0000012.

References

1 L.D. Zhao, V. P. Dravid and M. G. Kanatzidis, *Energy & Environmental Science*, 2014, **7**, 251.
2 X.Zhang and L.D. Zhao, *J. Materiomics*, 2015, **1**, 92-105.
3 Y. Pei, X. Shi, A. LaLonde, H. Wang, L. Chen and G. J. Snyder, *Nature*, 2011, **473**, 66-69.
4 D. J. Chadi, *Physical Review B*, 1977, **16**, 1746-1747.
5 J. P. Heremans, V. Jovovic, E. S. Toberer, A. Saramat, K. Kurosaki, A. Charoenphakdee, S. Yamanaka and G. J. Snyder, *Science*, 2008, **321**, 554-557.
6 L. D. Zhao, J. He, S. Hao, C. I. Wu, T. P. Hogan, C. Wolverton, V. P. Dravid and M. G. Kanatzidis, *Journal of the American Chemical Society*, 2012, **134**, 16327-16336.
7 T. Takabatake, K. Suekuni and T. Nakayama, *Reviews Of Modern Physics*, 2014, **86**, 669-716.
8 X. Lu, D. T. Morelli, Y. Xia, F. Zhou, V. Ozolins, H. Chi, X. Zhou and C. Uher, *Advanced Energy Materials*, 2013, **3**, 342-348.

9 M. S. Dresselhaus, G. Chen, M. Y. Tang, R. G. Yang, H. Lee, D. Z. Wang, Z. F. Ren, J. P. Fleurial and P. Gogna, *Advanced Materials*, 2007, **19**, 1043-1053.

10 L. D. Zhao, S. H. Lo, Y. Zhang, H. Sun, G. Tan, C. Uher, C. Wolverton, V. P. Dravid and M. G. Kanatzidis, *Nature*, 2014, **508**, 373-377.

11 J. D. Wasscher, W. Albers and C. Haas, *Solid State Electron*, 1963, **6**, 261-264.

12 J. S. Rhyee, K. H. Lee, S. M. Lee, E. Cho, S. Il Kim, E. Lee, Y. S. Kwon, J. H. Shim and G. Kotliar, *Nature*, 2009, **459**, 965-968.

13 T. Chattopadhyay, J. Pannetier and H. G. Vonschnering, *J Phys Chem Solids*, 1986, **47**, 879-885.

14 A. S. Pashinkin, A. S. Malkova, V. A. Fedorov and M. S. Mikhailova, *Inorg Mater+*, 2006, **42**, 593-595.

15 I. A. Smirnov, Vinograd.Mn, Kolomoet.Nv and L. M. Sysoeva, *Fiz Tverd Tela+*, 1968, **9**, 2074.

16 L. D. Zhao, H. J. Wu, S. Q. Hao, C. I. Wu, X. Y. Zhou, K. Biswas, J. Q. He, T. P. Hogan, C. Uher, C. Wolverton, V. P. Dravid and M. G. Kanatzidis, *Energy & Environmental Science*, 2013, **6**, 3346-3355.

17 P. E. Blochl, *Physical Review B*, 1994, **50**, 17953-17979.

18 G. Kresse and D. Joubert, *Physical Review B*, 1999, **59**, 1758-1775.

19 G. Kresse and J. Furthmuller, *Physical Review B*, 1996, **54**, 11169-11186.

20 J. P. Perdew, K. Burke and M. Ernzerhof, *Physical Review Letters*, 1996, **77**, 3865-3868.

21 M. Cutler and N. F. Mott, *Physical Review*, 1969, **181**, 1336-1340.

22 Y. Z. Pei, H. Wang and G. J. Snyder, *Advanced Materials*, 2012, **24**, 6125-6135.

23 C. M. Jaworski, M. D. Nielsen, H. Wang, S. N. Girard, W. Cai, W. D. Porter, M. G. Kanatzidis and J. P. Heremans, *Physical Review B*, 2013, **87**, 045203.

24 W. Liu, X. J. Tan, K. Yin, H. J. Liu, X. F. Tang, J. Shi, Q. J. Zhang and C. Uher, *Physical Review Letters*, 2012, **108**.

25 S. Asanabe, *J Phys Soc Jpn*, 1959, **14**, 281-296.

26 K. Biswas, J. He, I. D. Blum, C. I. Wu, T. P. Hogan, D. N. Seidman, V. P. Dravid and M. G. Kanatzidis, *Nature*, 2012, **489**, 414-418.

27 W. Liu, H. Chi, H. Sun, Q. Zhang, K. Yin, X. F. Tang, Q. J. Zhang and C. Uher, *Phys Chem Chem Phys*, 2014, **16**, 6893-6897.

28 G. J. Tan, W. Liu, S. Y. Wang, Y. G. Yan, H. Li, X. F. Tang and C. Uher, *Journal Of Materials Chemistry A*, 2013, **1**, 12657-12668.

29 S. Il Kim, K. H. Lee, H. A. Mun, H. S. Kim, S. W. Hwang, J. W. Roh, D. J. Yang, W. H. Shin, X. S. Li, Y. H. Lee, G. J. Snyder and S. W. Kim, *Science*, 2015, **348**, 109-114.

30 D. R. Clarke, *Surf Coat Tech*, 2003, **163**, 67-74.

31 J. Shuai, H. S. Kim, Y. C. Lan, S. Chen, Y. Liu, H. Z. Zhao, J. H. Sui and Z. F. Ren, *Nano Energy*, 2015, **11**, 640-646.

32 H. J. Wu, L. D. Zhao, F. S. Zheng, D. Wu, Y. L. Pei, X. Tong, M. G. Kanatzidis and J. Q. He, *Nat Commun*, 2014, **5,** 4515.

33 E. M. Levin, S. L. Bud'ko and K. Schmidt-Rohr, *Adv Funct Mater*, 2012, **22**, 2766-2774.

34 X. Shi, J. Yang, J. R. Salvador, M. F. Chi, J. Y. Cho, H. Wang, S. Q. Bai, J. H. Yang, W. Q. Zhang and L. D. Chen, *Journal of the American Chemical Society*, 2011, **133**, 7837-7846.

35 S. Perumal, S. Roychowdhury, D. S. Negi, R. Datta, and K. Biswas, *Chem. Mater.* 2015, **27**, 7171–7178.

36 K. F. Hsu, S. Loo, F. Guo, W. Chen, J. S. Dyck, C. Uher, T. Hogan, E. K. Polychroniadis and M. G. Kanatzidis, *Science*, 2004, **303**, 818-821.

37 C. G. Fu, S. Q. Bai, Y. T. Liu, Y. S. Tang, L. D. Chen, X. B. Zhao and T. J. Zhu, *Nat Commun*, 2015, **6**, 8144.

38 L. D. Zhao, G. J. Tan, S. Q. Hao, J. Q. He, Y. L. Pei, H. Chi, H. Wang, S. K. Gong, H. B. Xu, V. P. Dravid, C. Uher, G. J. Snyder, C. Wolverton and M. G. Kanatzidis, *Science*, 2015, DOI: 10.1126/science.aad3749.